Updated Airborne Multipath Models for Dual-frequency Multi-constellation GBAS

Maria Caamano, Daniel Gerbeth, Stefano Caizzone, *German Aerospace Center (DLR)*
Matteo Sgammini, *European Commission, Joint Research Centre (JRC)*

BIOGRAPHY

Maria Caamano received a Master's degree in Telecommunications engineering from the University of Oviedo, Spain, in March 2015, and a PhD in Aerospace Science and Technology from the Polytechnic University of Catalonia (UPC), Spain, in July 2022. Since May 2015, she has been working as a research associate at the Institute of Communications and Navigation at the German Aerospace Center (DLR). Her work focuses on the development of dual-frequency multi-constellation Ground Based Augmentation Systems (GBAS).

Daniel Gerbeth received his Bachelor's and Master's degrees in Electrical Engineering and Information Technology from the Karlsruhe Institute of Technology, Germany, in 2014. During his master studies he specialized in aerospace technology and navigation. After working in the field of sensor fusion and navigation aiding at Fraunhofer IOSB, he joined the German Aerospace Center (DLR) in May 2015 and has since been involved in research on Ground Based Augmentation Systems (GBAS) and reliable navigation for urban air mobility.

Stefano Caizzone received the M.Sc. in Telecommunications Engineering and the Ph.D. degree in Geoinformation from the University of Rome "Tor Vergata", Italy, in 2009 and 2015, respectively. Since 2010, he is with the Antenna group of the German Aerospace Center (DLR), where he has been responsible for the development of innovative miniaturized antennas. Since July 2020, he leads the Antenna Systems Group. His main research interests concern small antennas for satellite navigation, controlled radiation pattern antennas for robust satellite Navigation and high-performance antenna design for precise satellite navigation, antenna arrays for satellite communication and installed performance analysis.

Matteo Sgammini is a technical officer at the Joint Research Centre (JRC) of the European Commission. He was a system and software engineer at MTU Aero Engines from 2006 to 2008. From September 2008 to April 2017 he was a research associate in the Navigation group of the Institute of Communication and Navigation at the German Aerospace Center (DLR), Germany. His research includes signal processing and estimation theory for GNSS. Currently he focuses on GNSS integrity, Galileo Safety-of-Life services, and Galileo system performance verification.

ABSTRACT

Currently proposed airborne multipath models are based on 100-second time-invariant (for single-frequency L1/E1 and L5/E5a signals) and time-variant (for the ionospheric-free combination of these signals) smoothing to describe the behavior of the aiborne multipath error in different applications (e.g. Satellite Based Augmentation Systems and Advance Receiver Autonomous Integrity Monitoring). However, the recently proposed architecture for dual-frequency multi-constellation (DFMC) Ground-Based Augmentation Systems (GBAS) incorporates different smoothing characteristics, as the use of divergence-free time-variant smoothing also for L1/E1 and L5/E5a with time constants ranging from raw data up to 600 seconds.

Therefore, this paper presents extended airborne multipath models for single-frequency GPS and Galileo L1/E1, L5/E5a, and the ionospheric-free combination to support standardization of DFMC GBAS. To derive these models, data collected during dedicated flight campaigns within the European project DUFMAN (Dual Frequency Multipath Model for Aviation) has been re-processed using a methodology similar to that employed in the DUFMAN project itself. This methodology involves estimating multipath from divergence-free code-minus-carrier observables, removing cycle slips, calibrating airborne antenna errors, and resolving ambiguities. Additionally, the behavior of estimated multipath during the transient phase of the time-variant filter is studied.

The results include proposed models for both unsmoothed and 600-second smoothed multipath after filter convergence, as well as inflation factors to adjust the proposed 600-second model to account for increased errors during the filter's transient phase.

I. INTRODUCTION

Aeronautical navigation has evolved significantly with the increasing reliance on Global Navigation Satellite Systems (GNSS). GNSS serves as a crucial component of performance-based navigation, allowing airspace users to ensure that their navigation capabilities meet the required levels of integrity, accuracy, continuity, and availability during the different phases of flight. To meet these performance requirements, a range of techniques and augmentation systems has been developed, including Aircraft Based Augmentation Systems (ABAS), Space Based Augmentation Systems (SBAS), and Ground Based Augmentation Systems (GBAS).

In ABAS, GNSS augmentation is entirely performed on the aircraft, which is fully responsible for integrity monitoring (Radio Technical Commission for Aeronautics (2020)). SBAS uses a network of accurately located ground reference stations spread over continental regions to compute integrity and correction information for one or more primary GNSS constellations. This information is then broadcast to the covered area using geostationary (GEO) satellites (Radio Technical Commission for Aeronautics (2020)). GBAS is a local area, airport-based differential GNSS that also supports one or more primary GNSS constellations. A GBAS reference station broadcasts differential corrections along with integrity parameters to the aircraft. GBAS is currently the only GNSS-based system that can support approaches under Category III (CAT III) weather conditions, including automatic landings (Radio Technical Commission for Aeronautics (2018a)).

With the introduction of a second frequency (L5/E5a) usable for civil aviation and the development of multiple satellite constellations (e.g., Galileo), the mentioned augmentation systems continue to be developed to enhance performance. ABAS is evolving towards the Advanced Receiver Autonomous Integrity Monitoring (ARAIM) concept, which leverages dual-frequency measurements to remove the first order ionospheric delay error. The European SBAS, known as European Geostationary Navigation Overlay Service (EGNOS), will provide augmentation for both the Galileo and GPS constellations on two frequencies in its V3 phase. On the GBAS side, the development of a dual-frequency and multi-constellation architecture is ongoing to address challenges posed by the active ionosphere in equatorial regions.

All these GNSS augmentation systems require that both fault-free errors and undetected faults are bounded by an integrity limit with a probability sufficient to support safety-of-life operations. One significant fault-free error source, particularly for high-accuracy operations such as precision approach and landing, is airborne multipath. Airborne multipath refers to pseudorange measurement errors caused by GNSS signals received from direct satellite line-of-sight mixed with reflections of those signals in different parts of the airframe (e.g. wings or tail).

The impact of airborne multipath on the GPS L1 C/A signal was previously characterized, leading to the development and validation of multipath error models based on data from dedicated flight campaigns (Wozniak and Murphy (1997); Booth et al. (2000); Murphy et al. (2005a,b)). These models represent the steady-state error for 100-second carrier-smoothed pseudorange measurements, derived from the standard deviation of data grouped by elevation. The approach relies on the assumption that when various error sources are combined for each pseudorange and then combined again in the position solution, the overall error distribution will approximate a Normal distribution. The resulting models are used to calculate protection levels (i.e. position error integrity bounds) for the various augmentation systems (International Civil Aviation Organization (2017)). This is achieved by combining the standard deviations of all pseudorange error sources through a root-sum-square method, projecting the combined result into the position domain, and applying a bounding k-factor. This k-factor, typically around six standard deviations, corresponds to the integrity probability required to ensure safety.

However, for a while, there were no airborne multipath error models for the new signals and constellations. To address this gap, the European Commission (EC) funded the Dual Frequency Multipath Model for Aviation (DUFMAN) project from 2018 to 2021 under the Horizon 2020 R&D Framework Program, with support from the EC Joint Research Centre (JRC). One significant outcome of this project was the proposal to separate actual multipath errors from additional errors introduced by the receiver antenna, specifically antenna group delay variations (AGDV), which were previously included in the multipath estimation (Circiu et al. (2020a, 2021)). The reason behind is that antenna errors can differ significantly between antennas and vary with the antenna's installation, signal frequency, and angle of arrival of the signal (Caizzone et al. (2017)). In the models for GPS L1, these errors were grouped with multipath and noise errors and bounded within the multipath model. This approach had limitations, as it made the results highly dependent on the antenna used, leading to models that could be either overly conservative (with low-performance antennas) or too optimistic (with high-performance antennas), thus inadequately bounding the errors. Additional testing confirmed that the GPS L1 standard airborne multipath model still effectively bounded these error sources, including group delay variations, in the position domain (Harris et al. (2017)). However, despite of this and the GPS antenna Minimum Operational Performance Standards (MOPS) requiring limits on antenna errors (Radio Technical Commission for Aeronautics (2006, 2018b)), it was agreed that separating the multipath and antenna contributions would be beneficial. This separation would provide more flexibility when different antennas are used, ensuring more accurate and reliable error modeling.

Therefore, the primary objective of the DUFMAN project was to develop airborne multipath and Antenna Group Delay Variation (AGDV) error models tailored for dual-frequency and dual-constellation applications, specifically targeting Galileo E1/E5a and GPS L1/L5 frequencies (Circiu et al. (2021); Sgammini et al. (2022a)). While the project primarily focused on Dual Frequency Multi-Constellation (DFMC) SBAS, the derived models also found applicability in DFMC GBAS and ARAIM. In the case of GBAS, the DUFMAN models were applicable to one of the potential architectures proposed for future DFMC GBAS (so-called

GBAS Approach Service Type (GAST) F), which was based on sending 100-seconds smoothed pseudorange corrections from the ground station for both GPS and Galileo and L1/E1 and L5/E5a signals (Durba (2018)).

Additionally, Harris et al. (2020) derived airborne multipath models for GPS L1, Galileo E1, GPS L5, and Galileo E5a using data from dedicated flight campaigns conducted with an experimental installation on a Boeing 777 airplane, employing the same airborne receiver prototype used in DUFMAN. The results from this study showed higher multipath models compared to those produced in DUFMAN, even exceeding the GPS L1 standard model in some elevations. This discrepancy can be attributed to several factors. The primary reason appears to be that Harris et al. (2020) used an electromagnetic (EM) model of the antenna group delay variation (AGDV) to remove the antenna effect, rather than the actual AGDV measured from an anechoic chamber. This EM model, being optimistic, resulted in less antenna contribution being subtracted. Additionally, the placement of the antennas on the Boeing 777 might have contributed to increased susceptibility to multipath, compared to the configuration used in DUFMAN. Furthermore, the study in Harris et al. (2020) computed models that overbounded the tails of the multipath distribution per elevation bin, whereas the DUFMAN's models are based on root-mean-square (RMS) values and do not use bounds for the tails, as these are assumed to be accounted for when computing protection levels. The final conclusion drawn from the study by Harris et al. (2020) is that additional research is required to identify the underlying causes of the discrepancies between the different models and to establish a consensus on a standardized method for deriving these models, including considerations such as whether to incorporate tail bounds or not.

In 2020, an alternative DFMC GBAS architecture, known as GAST X, that significantly changed the way in which traditional GBAS was working, was proposed. GAST X proposed to send all relevant raw measurements to the aircraft, allowing different types of processing to compute the aircraft's position, such as Divergence-free (Dfree) combinations of L1/E1 and L5/E5a signals with longer smoothing time constants (Murphy et al. (2021)).

In recent developments, the ICAO GBAS Working Group (GWG), responsible for establishing standards for the DFMC GBAS, has consolidated the previously separate proposed architectures into a unified DFMC GBAS architecture known as GAST E. This new architecture is currently undergoing trade studies to determine the most suitable overall design, fallback modes, and the Concept of Operations (ConOps) for DFMC GBAS. The selected architecture is anticipated to utilize time-variant smoothing for code measurements on L1/E1, using the divergence-free combination of carrier-phases computed with L1/E1 and L5/E5a. Additionally, ionospheric monitors will be implemented, particularly on the airborne side, to detect when satellites are impacted by ionospheric gradients. If the number of affected satellites becomes substantial, rendering the nominal Dfree mode unfeasible, the system will switch to an ionosphere-free (Ifree) mode. In this mode, ionosphere-free combinations of smoothed code measurements will be used to eliminate the first-order ionospheric error. Furthermore, a range of fallback modes is proposed to ensure continued operation in scenarios such as losing one frequency. These fallback modes include support for Category III (Cat III) operations using only L1/E1 or L5/E5a frequencies.

Given that the newly introduced GAST E architecture is expected to employ divergence-free (Dfree) time-variant smoothing with both shorter and longer smoothing time constants, as opposed to the previously proposed single-frequency time-invariant smoothing filters with a 100-second time constant in GAST F, it is necessary to expand the existing airborne multipath models. This expansion will incorporate the specific processing characteristics of GAST E that are not accounted for in the current models. Addressing these aspects is crucial for resolving integrity concerns and mitigating the effects of overly conservative multipath models, which could potentially impact service availability.

In this work, we present an update of the existing airborne multipath models, integrating the specific particularities of the GAST E architecture. Our approach involves a comprehensive re-processing of the data collected within the DUFMAN project, taking into account the revised processing methodology to investigate the impact of changing the traditional 100-second smoothing to a divergence-free time-variant smoothing scheme, incorporating smoothing time constants from 0 to up to 600 seconds. Additionally, inflation factors to take into account the potential use of measurements during the transient phase of the filters (i.e., before filter convergence to the steady state) are derived. The update of the existing airborne models has been carried out as part of the project EGNSS DFMC for GBAS Based Operations (EDGAR), which is co-funded by the European Union under the Horizon Europe funding program.

This paper is structured as follows: Section II describes the data used for this study, Section III describes the methodology followed to derive the updated airborne multipath models, Section IV describes the methodology to derive an inflation factor for the transient phase of the filters, and Section V presents the results for both the updated models and the study on the multipath behaviour during the transient phase of the filters.

II. DATA

The DUFMAN dataset includes data from various aircraft types, such as the Airbus A320, A321, A330-900, and A350, all equipped with a multiband antenna compliant with MOPS DO-373 (Radio Technical Commission for Aeronautics (2018b)), installed in the primary GPS 2 location. This antenna was characterized in DLR's anechoic chamber before being installed on the aircraft.

Additionally, other antennas were analyzed and tested in the lab to compute different references for antenna group delay variations and provide a broader range of expected performance for commercial antennas. One of these lab-tested antennas, different from the one used in flight trials, was selected to characterize the worst-case code errors introduced by antenna group delay variations (AGDV errors) (Circiu et al. (2021); Sgammini et al. (2022b)).

For data recording in all installations, a data grabber was used to record baseband samples for a later replay in the lab. The Multi Mode Receiver (MMR) used for replay and the analysis was the Collins GLU-2100, a dual frequency and multi constellation MMR prototype capable of tracking GPS L1, GPS L5, Galileo E1 and Galileo E5a signals. Chip spacing and bandwidth were compliant with the MOPS for Galileo/GPS SBAS Airborne Equipment (ED-259, Eurocae (2019)). More information regarding the flight campaigns and data collected in the DUFMAN project can be found in Circiu et al. (2021, 2020b, 2019).

For the derivation of the updated airborne multipath models, we used only data from in-flight and approach phases, with low-quality data being excluded. We adopted this approach because using ground data and low-quality data would typically result in higher multipath models, which could be excessively conservative for standard aircraft and GBAS operations. Consequently, the newly derived models are based on approximately 21 flight hours of data. Figure 1 shows the number of "unsmoothed" or "raw" samples used in this work. It is important to note that, should DFMC GBAS (i.e., GAST E) be used for providing guidance during taxi or parking, dedicated airborne models specific to these operational phases would need to be developed.

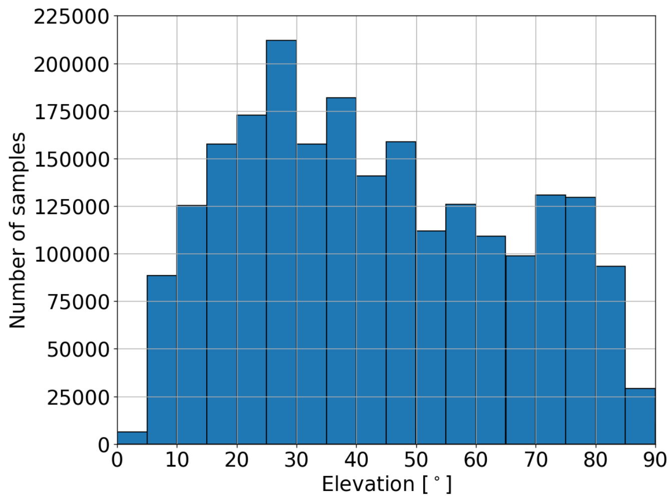

Figure 1: Number of "unsmoothed" samples used for GPS and Galileo together.

III. METHODS

As outlined in Section I, the DUFMAN project proposed dividing the residual pseudorange airborne errors, typically characterized by the $\sigma_{pr,air}$ error term used in the computation of protection levels (Radio Technical Commission for Aeronautics (2018a)), into distinct error contributions: airborne multipath (σ_{MP}), airborne receiver thermal noise (σ_{th}), and antenna group delay variation (σ_{AGDV}). The final model is computed as:

$$\sigma_{pr,air} = \sqrt{\sigma_{MP}^2 + \sigma_{th}^2 + \sigma_{AGDV}^2}. \tag{1}$$

The contribution of the antenna group delay variation was derived in the DUFMAN project (Circiu et al. (2021)). While further studies are needed to confirm that the model for AGDV remains unaffected by the new processing scheme, this aspect is beyond the scope of the current paper and will be addressed in future work.

For the noise contribution, various models can be applied. Typically, the noise part of the Airborne Accuracy Designator B (AAD B) model, which represents the performance of advanced receiver technologies with narrow-correlator spacing, is utilized (see Section 3.6.8.2 of International Civil Aviation Organization (2017)).

Therefore, this work focuses exclusively on the update of the airborne multipath models (σ_{MP}). The process of estimating multipath for each GNSS signal and their ionospheric-free combinations involves several key steps. In the following sections, we provide a detailed explanation of each step.

1. Estimation of multipath and noise

A commonly used methodology to assess the multipath and noise errors contained in the single-frequency pseudorange measurements is the study of the behavior of the Code-Minus-Carrier (CMC) observable (Braasch (1994)).

The code (pseudorange) and carrier-phase measurements for a single receiver r, frequency i , satellite s, and epoch k can be described by:

$$\begin{aligned}\rho^s_{r,i,k} &= R^s_{r,k} + c\cdot(\delta t_{r,k} - \delta t^s_k) + I^s_{r,i,k} + T^s_{r,k} + MP^s_{r,i,k} + \epsilon^s_{r,i,k} + B^s_{i,k} + B_{r,i,k} + \xi^s_{i,k} + \xi_{r,i,k} + e^s_{r,i,k},\\ \phi^s_{r,i,k} &= R^s_{r,k} + c\cdot(\delta t_{r,k} - \delta t^s_k) - I^s_{r,i,k} + T^s_{r,k} + mp^s_{r,i,k} + \eta^s_{r,i,k} + N^s_{r,i,k}\cdot\lambda_i + \beta^s_{i,k} + \beta_{r,i,k} + \zeta^s_{i,k} + \zeta_{r,i,k} + e^s_{r,i,k} + wu^s_{\phi,r,i,k},\end{aligned} \tag{2}$$

where $R^s_{r,k}$ is the geometrical satellite-user range (in meters), c is the speed of light (in m/s), $\delta t_{r,k}$ and δt^s_k are the user and satellite clock biases respectively (in seconds), $I^s_{r,i,k}$ is the ionospheric delay (in meters), $T^s_{r,k}$ is the tropospheric delay (in meters), and $N^s_{r,i,k}$ and λ_i are the integer ambiguity (in cycles) and the corresponding wavelength of the frequency i. Additionally, $MP^s_{r,i,k}$, $\epsilon^s_{r,i,k}$ and $mp^s_{r,i,k}$, $\eta^s_{r,i,k}$, represent the multipath and thermal noise errors in the code and carrier-phase measurements all in meters, respectively. Finally, $B^s_{i,k}$ and $B_{r,i,k}$ represent the pseudorange satellite and receiver instrumental errors (in meters), $\beta^s_{i,k}$ and $\beta_{r,i,k}$ represent the carrier-phase satellite and receiver instrumental errors (in meters), the terms $\xi^s_{i,k}, \xi_{r,i,k}$ and $\zeta^s_{i,k}, \zeta_{r,i,k}$ describe the errors introduced by the satellite and receiver antenna on pseudorange measurements and on carrier-phase measurements (in meters), respectively, the $wu^s_{\phi,r,i,k}$ refers to the phase windup error (in meters), and $e^s_{r,i,k}$ represents the ephemeris errors (in meters).

The CMC can be built as the difference of both code and carrier-phase measurements as:

$$\begin{aligned}CMC^s_{r,i,k} &= \rho^s_{r,i,k} - \phi^s_{r,i,k}\\ &= 2\cdot I^s_{r,i,k} + (MP^s_{r,i,k} + \epsilon^s_{r,i,k} + B^s_{i,k} + B_{r,i,k} + \xi^s_{i,k} + \xi_{r,i,k}) -\\ &\quad - (mp^s_{r,i,k} + \eta^s_{r,i,k} + N^s_{r,i,k}\cdot\lambda_i + \beta^s_{i,k} + \beta_{r,i,k} + \zeta^s_{i,k} + \zeta_{r,i,k} + wu^s_{\phi,r,i,k}).\end{aligned} \tag{3}$$

This combination removes the clock errors, the tropospheric delay and the ephemeris error. However, it contains twice the ionospheric delay, the carrier phase ambiguity term, the code and carrier-phase multipath and noise, the code and carrier phase hardware delays (i.e, instrumental delays and antenna errors), and the phase windup error. Therefore, the CMC as defined in Equation (3) cannot be used directly to assess the code multipath present in the GNSS measurements.

In this step, the first order of the ionospheric delay error can be estimated and removed by combining carrier-phase measurements in two different frequencies f_i and f_j as:

$$\hat{I}^s_{r,i,k} = \frac{f_j^2}{f_i^2 - f_j^2}\left(\phi^s_{r,i,k} - \phi^s_{r,j,k}\right). \tag{4}$$

By subtracting two times the result of Equation (4) from Equation (3), we obtain the Code-Minus-Carrier measurements with the ionospheric divergence removed that we call CMC divergence free with biases ($CMC_{\mathit{Dfree,\ bias}}$). The reason behind is that using the carrier-phase measurements to estimate the ionospheric delay introduces a linear combination of the carrier-phase ambiguities from the two frequencies in addition to the hardware biases and the single-frequency carrier-phase ambiguity mentioned before. The $CMC_{\mathit{Dfree,\ bias}}$ can be therefore described as:

$$\begin{aligned}CMC^s_{\text{Dfree,bias,r,i,k}} &= (MP^s_{r,i,k} + \epsilon^s_{r,i,k} + B^s_{i,k} + B_{r,i,k} + \xi^s_{i,k} + \xi_{r,i,k}) - (mp^s_{r,i,k} + \eta^s_{r,i,k} + \beta^s_{i,k} + \beta_{r,i,k} + \zeta^s_{i,k} + \zeta_{r,i,k}) -\\ &\quad - \frac{2\cdot f_j^2}{f_i^2 - f_j^2}\cdot\left(mp^s_{r,i,k} + \eta^s_{r,i,k} + \beta^s_{i,k} + \beta_{r,i,k} + \zeta_{r,i,k} + \zeta^s_{i,k} - mp^s_{r,j,k} - \eta^s_{r,j,k} - \beta^s_{j,k} - \beta_{r,j,k} - \zeta_{r,j,k} - \zeta^s_{j,k}\right) -\\ &\quad - N^s_{r,i,k}\cdot\lambda_i - \frac{2\cdot f_j^2}{f_i^2 - f_j^2}\cdot\left(N^s_{r,i,k}\cdot\lambda_i - N^s_{r,j,k}\cdot\lambda_j\right) - wu^s_{\phi,r,i,k} - \frac{2\cdot f_j^2}{f_i^2 - f_j^2}\cdot\left(wu^s_{\phi,r,i,k} - wu^s_{\phi,r,j,k}\right).\end{aligned} \tag{5}$$

Since the carrier-phase multipath and noise are orders of magnitude smaller than the code multipath and noise errors, a common assumption is to consider both the carrier-phase noise and multipath negligible compared to the code ones ($mp^s_{i,k} << MP^s_{i,k}$ and $\zeta^s_{i,k} << \epsilon^s_{i,k}$) (Misra and Enge (2006)). Still, the $CMC_{\mathit{Dfree,\ bias}}$ as defined in Equation (5) cannot be used directly to assess the code multipath present in the GNSS measurements, since it contains the integer ambiguity terms, hardware biases and phase windup errors.

When using measurements from flight data, accurately estimating carrier-phase ambiguities becomes challenging due to the aircraft's movement and the increased frequency of cycle slips and loss-of-lock events, which are more common than in static ground data. These frequent cycle slips can result from rapid changes in the satellite's elevation and azimuth angles, as well as signal blockages during aircraft maneuvers. Additionally, any errors in calculating the ambiguities and hardware biases can lead to inaccuracies in multipath estimations. Section III.5 explains the selected method to remove carrier-phase ambiguities and constant hardware biases, Section III.4 explains the method to remove antenna errors, and Section III.3 explains the method to remove the phase windup error. The result after ambiguities, hardware biases and phase windup removal can be considered as the estimation of the single-frequency code noise and multipath denoted as CMC_{Dfree}.

Furthermore, it is of interest to also have an estimate of the multipath of the ionospheric-free combination of GNSS signals (e.g. L1/E1 and L5/E5a), as the ionospheric-free mode is proposed to be a fallback mode for GAST E in case there is very high ionospheric activity as explained in Section I.

In this case, the multipath present in the ionospheric-free pseudorange combination can be estimated by forming the ionospheric-free combination on the single-frequency CMC_{Dfree} (the estimate after the ambiguities removal) as:

$$CMC^{s}_{Ifree,r,k} = \frac{f_i^2 \cdot CMC^{s}_{Dfree,r,i,k} - f_j^2 \cdot CMC^{s}_{Dfree,r,j,k}}{f_i^2 - f_j^2}. \tag{6}$$

2. Cycle slip detection

In the estimation of multipath and noise errors, detecting cycle slips is crucial. Receiver loss of lock results in discontinuities in carrier phase measurements, manifesting as jumps of integer multiples of the frequency wavelength (cycle slips). Various algorithms for cycle slip detection are available, utilizing either single-frequency or dual-frequency measurements, and either carrier phase alone or both code and carrier phase measurements to identify these jumps.

Ideally, the same cycle slip detectors used in the processing of the GNSS signals in certified airborne receivers should be employed for deriving multipath models. However, different manufacturers may implement different cycle slip detection strategies. Also, in some cases, the strategy might be to repair as much cycle slips as possible when detected, while in other cases, the strategy might be to always restart the smoothing filters whenever a cycle slip is detected. Despite these variations, the consensus in the community is to remove cycle slips from the data as much as possible to replicate the functionality of airborne receivers.

Therefore, in this paper, we use different cycle slip detectors in order to detect and remove these jumps from the data. Firstly, we set a limit for Carrier-to-Noise Ratio (C/N0) at 29 dB-Hz for L1/E1 and 27 dB-Hz for L5/E5a to remove low quality data, following the DUFMAN project's recommendations (Circiu et al. (2021)). Then, the Measurement Quality Monitor (MQM), as detailed in Section 2.3.6.7 of Radio Technical Commission for Aeronautics (2018a), is employed. Instead of the 10 meters threshold suggested in the standards, empirical thresholds of 5 meters for L1/E1 and 3 meters for L5/E5a are used based on the used dataset.

Secondly, a single-frequency cycle slip detector is utilized, which relies on the difference between code and phase measurements. This detector calculates the difference between the changes in code measurements and phase measurements over two consecutive epochs, comparing it with a threshold of 5 meters. This approach is applied per frequency.

Finally, a dual-frequency cycle slip detector is implemented, utilizing code and carrier phase measurements through the Melbourne-Wübbena combination. Described in Section 4.3.1.2 of Sanz et al. (2013), this algorithm provides a noisy estimate of the wide-lane ambiguity by calculating the difference between the wide-lane combination of carrier phase measurements and the narrow-lane combination of code measurements. The detector algorithm uses this difference, with detection based on real-time computation of the mean and standard deviation of the observables. A cycle slip is flagged when the difference exceeds a predefined number of standard deviations (e.g., 5) from the predicted mean value.

When a cycle slip detector is triggered, the smoothing filters are restarted, and the specific code and carrier-phase measurements are removed, without repairing the cycle slip. This conservative strategy ensures that the data used for deriving multipath models is free from remaining or incorrectly repaired cycle slips, leading to models that accurately reflect the behavior of airborne GNSS receivers.

After removing cycle slips and assuming that carrier-phase multipath and noise are negligible due to being orders of magnitude smaller than pseudorange errors, the $CMC^{s}_{\mathrm{Dfree,bias,r,i,k}}$ samples from Equation (5) still present certain errors. These errors can be categorized into two types. First, there are errors considered constant over time, including the code and carrier-phase receiver instrumental errors ($B_{r,i,k}$ and $\beta_{r,i,k}$, respectively), which are consistent across all satellites but vary between receivers, and the code and carrier-phase satellite instrumental errors ($B^{s}_{i,k}$ and $\beta^{s}_{i,k}$, respectively), which are consistent across receivers but vary between satellites. Second, there are time-varying errors, such as the code and carrier-phase antenna errors introduced by the receiver antenna ($\xi_{r,i,k}$ and $\zeta_{r,i,k}$, respectively), which vary with the GNSS signal's angle of arrival, the code and carrier-phase antenna errors introduced by the satellite antenna ($\xi^s_{i,k}$ and $\zeta^s_{i,j,k}$), which vary with the nadir angle, and the phase windup error ($wu^s_{\phi,r,i,k}$), which varies with the angle of arrival of the signal.

In Section III.3, we address the removal of the phase windup error, in Section III.4, we address the removal or calibration of antenna induced errors and, in Section III.5, we address the removal of the errors that are constant over time.

3. Carrier-phase windup error

Windup errors affect only the carrier phase measurements and arise from the electromagnetic nature of the circularly polarized waves used in GNSS signals. The impact of phase windup on these measurements depends on the orientation of both the transmitter's antenna (the satellite) and the receiver's antenna (the user), as well as the direction of the line of sight (see Sanz et al. (2013)).

For a static receiver, windup errors arise solely from the orbital motion of the satellite. However, during flight tests, the frequent changes in orientation between the satellite antenna and the airborne antenna result in more pronounced windup effects. These errors can significantly impact multipath estimation and must be accounted for (see Circiu (2020)). In Boeing (2005), a method is proposed to remove the phase windup error as:

$$\phi^s_{r,i,k} = \phi^s_{r,i,k} - \frac{\lambda_i}{2\pi} \cdot Az_{BF}, \tag{7}$$

with λ_i being the wavelength of the frequency i, and Az_{BF} being the azimuth angle of the satellite in radians with respect to aircraft's body frame. Note that for simplicity, we use the same symbol $\phi^s_{r,i,k}$ both before and after carrier-phase windup error correction. The carrier-phase measurements after carrier-phase windup error removal are the ones used for computing the $\mathit{CMC}^s_{r,i,k}$ samples in Equation (3).

4. Antenna error calibration

The satellite antenna introduces errors in the code and carrier-phase measurements. These errors vary with the nadir angle, as discussed by Wanninger et al. (2017). However, they are generally much smaller than the multipath errors and the errors introduced by the receiver antenna. These satellite antenna errors are typically not included in the derivation of multipath error models, as they are not considered dominant in the multipath estimation process (Circiu et al. (2020a)). Therefore, in this work, satellite antenna errors are considered negligible.

The receiver antenna introduces more significant errors in both code and carrier-phase measurements, which must be accounted for. One of these errors is the antenna group delay (AGD), defined as the "time-delay difference that each frequency component of the signal experiences while passing through the antenna" (Caizzone et al. (2019)). Ideally, the antenna's pattern would be isotropic within the frequency band of interest, resulting in a uniform group delay for all elevation and azimuth angles, thereby projecting only into the receiver clock. However, real-world antenna patterns deviate from this ideal, and the differential AGD is directly influenced by the uniformity of the antenna pattern, affecting the code measurements and varying with frequency, azimuth, and satellite elevation. Detailed derivations of AGD and its relationship with antenna gain and phase patterns are provided by Caizzone et al. (2017, 2019).

Additionally, phase center variation, which impacts carrier-phase measurements, introduces a phase contribution that varies with satellite elevation and azimuth, unrelated to the actual distance from the satellite but due to antenna characteristics (Caizzone et al. (2019)). While phase center variation errors are relatively small and primarily relevant to high-precision applications, AGD errors can reach meter levels and therefore must be considered.

During the DUFMAN project, a methodology was developed to derive the AGD and remove these antenna errors from the multipath estimation. A detailed explanation of this methodology can be found in Caizzone et al. (2019); Circiu et al. (2020a). As a summary, the antenna patterns were measured for each frequency in an anechoic chamber, and the code errors due to group delays were estimated by passing the antenna response function through an ideal receiver. The installed performance of an antenna on an aircraft, which alters the antenna radiation pattern, was approximated by measuring the antenna mounted on a rolled-edge ground plane. The results demonstrated that the estimated code error biases closely matched the actual errors observed in measurements (Caizzone et al. (2019)).

For this study, we re-measured the same antenna used in the DUFMAN flight campaigns in the DLR's compact anechoic chamber, obtaining more precise estimates of the antenna group delay. Figure 2 shows the code errors due to the absolute antenna group delays for GPS L1 C/A, Galileo E1, GPS L5, and Galileo E5a for all azimuth and elevation angles.

The absolute AGD refers to the total error introduced by the antenna, including the effects of its active components. This error is common across all satellites and, if uncorrected, projects into the receiver clock estimation. However, the critical aspect for

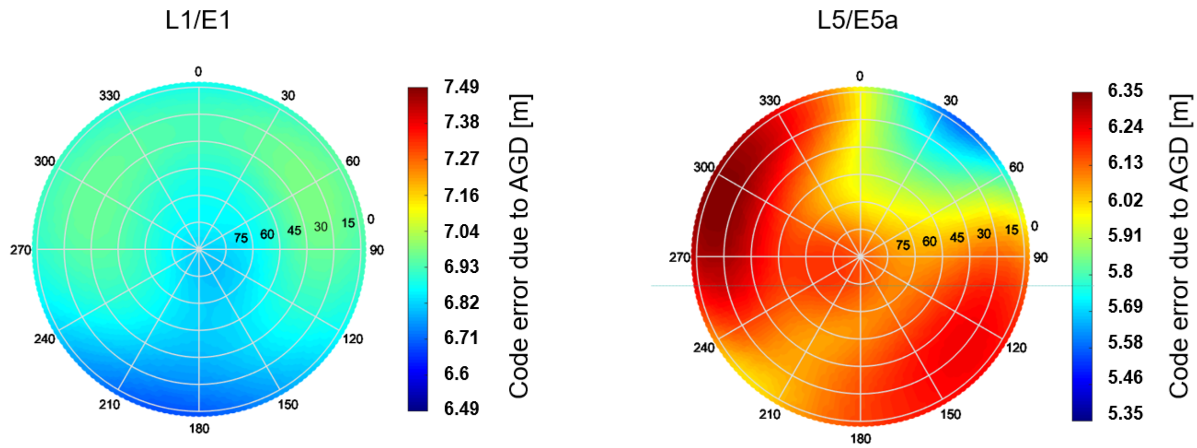

Figure 2: Code error due to the absolute AGD for GPS L1, Galileo E1, GPS L5, and Galileo E5a signals.

positioning accuracy is the variation in AGD across different satellite elevations and azimuths, referred to as the antenna group delay variation (AGDV).

Analysis of the antenna group delay reveals that the code errors induced by these variations differ across frequencies and exhibit significant changes depending on the angle of arrival. Specifically, variations up to 0.36 meters for L1/E1 and 1 meter for L5/E5a have been observed (see Figure 2), indicating a substantial spatial variation in the group delay across both frequencies.

Given the magnitude of these errors, several approaches can be employed to account for them. As discussed in the introduction, the standard procedure involves removing the antenna errors from the multipath estimation and then account for them in the model of the overall error as an additional error term (σ_{AGDV} in Equation (1)), obtained through a worst-case antenna still operating within the limits of the MOPS.

To effectively calibrate the antenna errors, it is essential to convert the satellite azimuth and elevation angles from Earth-Centered Earth-Fixed (ECEF) coordinates to aircraft body-fixed azimuth and elevation angles. This transformation requires accurate information on the aircraft's roll, pitch, and heading. The process begins by converting the ECEF coordinates into local North-East-Down (NED) coordinates using the following transformation:

$$\begin{bmatrix} x_{\text{NED}} \\ y_{\text{NED}} \\ z_{\text{NED}} \end{bmatrix} = \begin{bmatrix} -\sin(lat)\cdot\cos(lon) & -\sin(lat)\cdot\sin(lon) & \cos(lat) \\ -\sin(lon) & \cos(lon) & 0 \\ -\cos(lat)\cdot\cos(lon) & -\cos(lat)\cdot\sin(lon) & -\sin(lat) \end{bmatrix} \cdot \begin{bmatrix} x_{\text{ECEF}} \\ y_{\text{ECEF}} \\ z_{\text{ECEF}} \end{bmatrix} \tag{8}$$

where lat and lon represent the latitude and longitude in radians of the aircraft in WGS84 coordinates, respectively.

The NED coordinates are then transformed into the body frame coordinates by first performing a rotation by the third axis by the heading, then rotation around the second axis for the pitch, and finally by rotating the first axis by the roll as follows:

$$\begin{bmatrix} x_{\text{BF}} \\ y_{\text{BF}} \\ z_{\text{BF}} \end{bmatrix} = \begin{bmatrix} 1 & 0 & 0 \\ 0 & \cos(R) & \sin(R) \\ 0 & -\sin(R) & \cos(R) \end{bmatrix} \cdot \begin{bmatrix} \cos(P) & 0 & -\sin(P) \\ 0 & 1 & 0 \\ \sin(P) & 0 & \cos(P) \end{bmatrix} \cdot \begin{bmatrix} \cos(H) & \sin(H) & 0 \\ -\sin(H) & \cos(H) & 0 \\ 0 & 0 & 1 \end{bmatrix} \cdot \begin{bmatrix} x_{\text{NED}} \\ y_{\text{NED}} \\ z_{\text{NED}} \end{bmatrix} \tag{9}$$

with H, P, and R being the heading angle (from the true north), pitch angle, and the roll angle, respectively. The body-fixed coordinate system refers to the nose right-wing down coordinate frame. Finally, the elevation and azimuth angle in the body frame are obtained using the relation:

$$\begin{aligned} El_{BF} &= \arctan\left(\frac{-z_{BF}}{\sqrt{x_{BF}^2 + y_{BF}^2}}\right), \\ Az_{BF} &= \arctan\left(\frac{y_{BF}}{x_{BF}}\right), \end{aligned} \tag{10}$$

where a 0° elevation angle denotes the horizon and the 90°, the zenith. The azimuth angle is measured from 0° at the aircraft nose towards the right wing (which is 90°).

After performing this transformation, the AGDV errors for each frequency can be subtracted from the biased raw multipath estimation, denoted as $CMC^{s}_{\mathrm{Dfree,bias,r,i,k}}$ samples.

5. Removal of ambiguities

Figure 3 shows the $CMC_{\mathrm{Dfree,bias}}$ estimates for Galileo E1 after antenna error calibration during one of the DUFMAN flights. As can be seen, rather than forming continuous lines, the $CMC_{\mathrm{Dfree,bias}}$ for each of the satellites is divided into different segments. This segmentation is attributed to the carrier-phase ambiguities, which vary from one satellite to another and change whenever a cycle slip or loss of track occurs.

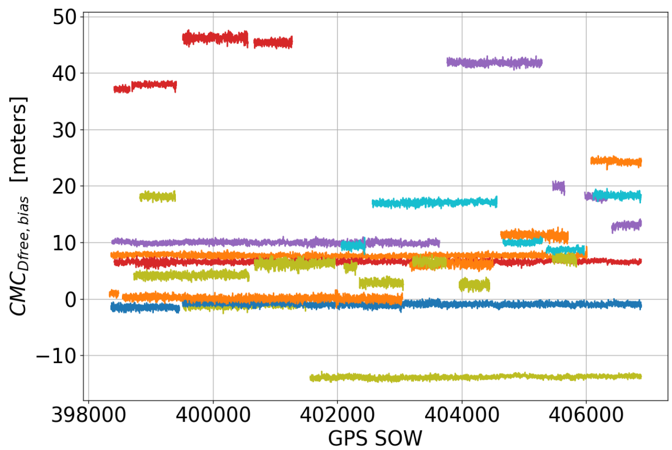

Figure 3: $CMC_{\mathrm{Dfree,bias}}$ estimates for Galileo E1 after antenna error calibration during one of the DUFMAN flights.

The input for the ambiguities removal algorithm is a continuous segment of unsmoothed $CMC_{\mathrm{Dfree,bias}}$ estimates for each satellite, during which the receiver maintains signal lock and no cycle slips occur. To ensure data quality, short data segments are excluded from consideration.

A common approach for estimating these ambiguities involves calculating the mean over a segment of continuous tracking for each satellite (Harris et al. (2020)). This method assumes that multipath errors follow a Gaussian distribution with a zero mean. Under low multipath conditions, this assumption is generally valid, and the mean provides a good estimate of the carrier-phase ambiguities.

However, this technique can inadvertently remove some constant multipath biases, particularly when large multipath errors are present. To address this, we compute the median over each satellite's continuous tracking segment instead of the mean, as the median is typically used as a more robust estimator. To ensure an accurate estimation of the ambiguities, we compute the median of $CMC_{\mathrm{Dfree,bias}}$ using only clean, high-quality, low-multipath measurements from in-flight observations (to avoid ground effects) with a C/N0 that exceeds 30 dB-Hz. These ambiguity estimations are then subtracted from the $CMC_{\mathrm{Dfree,bias}}$ per satellite and continuous segment.

After removing the median, all errors that can be considered constant over time, including code and phase instrumental errors and the constant part of the antenna biases, are also eliminated. Therefore, after this process, the only error terms remaining in CMC_{Dfree} are code multipath and thermal receiver noise.

While more sophisticated methods for estimating and removing ambiguities and constant errors have been proposed in the literature (Circiu et al. (2020a)), we selected the median removal process because it is significantly less complex, while producing analogous results.

6. Divergence-free time-variant smoothing

The next key step, which differs in part from the original DUFMAN study, involves passing the processed data through a code-carrier time-variant smoothing filter, employing the divergence-free processing mode and shorter/longer smoothing time constants.

The divergence-free smoothed pseudorange ($\overline{\rho}^s_{\text{Dfree},r,i,k}$) for receiver r, frequency i, satellite s, and epoch k can be expressed as:

$$\overline{\rho}^s_{\text{Dfree},r,i,k} = \alpha_k \cdot \rho^s_{r,i,k} + (1-\alpha_k) \cdot \left[\overline{\rho}^s_{\text{Dfree},r,i,k-1} + \phi^s_{\text{Dfree},r,i,k} - \phi^s_{\text{Dfree},r,i,k-1}\right], \tag{11}$$

where α_k is the weight that is given to the new measurement in meters, $\rho^s_{r,i,k}$ is the unsmoothed pseudorange measurement, and $\phi^s_{\text{Dfree},r,i,k}$ is the divergence-free carrier-phase measurement in meters computed as:

$$\phi^s_{\text{Dfree},r,i,k} = \phi^s_{r,i,k} - 2 \cdot \frac{f_j^2}{f_i^2 - f_j^2} \cdot (\phi^s_{r,i,k} - \phi^s_{r,j,k}), \tag{12}$$

where $\phi^s_{r,i,k}$ is the carrier-phase measurement in meters for frequency f_i and $\phi^s_{r,j,k}$ is the carrier-phase measurement in meters for frequency f_j.

Expanding the smoothing filter terms:

$$\overline{\rho}^s_{\text{Dfree},r,i,k} = \phi^s_{\text{Dfree},r,i,k} + (1-\alpha_k)^{k-1} \cdot \left(\rho^s_{\text{Dfree},r,i,1} - \phi^s_{\text{Dfree},r,i,1}\right) + \alpha_k \cdot \sum_{m=2}^{k} (1-\alpha_k)^{k-m} \cdot \left[\rho^s_{r,i,m} - \phi^s_{\text{Dfree},r,i,m}\right], \tag{13}$$

and rearranging the terms, we get:

$$\overline{\text{CMC}}^s_{\text{Dfree,bias,r,i,k}} = (1-\alpha_k)^{k-1} \cdot \left(\text{CMC}^s_{\text{Dfree,bias,r,i,1}}\right) + \alpha_k \cdot \sum_{m=2}^{k} (1-\alpha_k)^{k-m} \cdot \left[\text{CMC}^s_{\text{Dfree,bias, r,i,m}}\right]. \tag{14}$$

Consequently, if the biases are eliminated as described in the previous sections, the resulting expression is:

$$\overline{\text{CMC}}^s_{\text{Dfree,r,i,k}} = \alpha_k \cdot \text{CMC}^s_{\text{Dfree,r,i,k}} + (1-\alpha_k) \cdot \left[\overline{\text{CMC}}^s_{\text{Dfree,r,i,k-1}}\right]. \tag{15}$$

Therefore, filtering directly the $\text{CMC}^s_{\text{Dfree,r,i,k}}$ values is equivalent to filtering the pseudorange with the Hatch filter substracting the difference of divergence-free carrier-phases with the biases removed.

Regarding the use of time-variant filters as opposed to time-invariant filters, the main difference is that, in time-variant filters, the weight assigned to new measurements changes over time rather than remaining fixed:

$$\alpha_k = \begin{cases} \frac{\Delta t}{t} & \text{if } t < \tau \\ \frac{\Delta t}{\tau} & \text{if } t \geq \tau \end{cases} \tag{16}$$

Here, Δt is the observation sampling rate in seconds, t is the time elapsed since the start of the segment in seconds, and τ is the smoothing time constant in seconds. The advantage of time-variant filters over time-invariant filters is that it is possible to assume convergence to the steady state at 2τ rather than at 3.6τ. This allows for the use of smoothed measurements at an earlier stage.

7. Computation of statistics and removal of thermal receiver noise

After smoothing, the resultant $\overline{\text{CMC}}^s_{\text{Dfree,r,i,k}}$ samples provide an estimate of the smoothed multipath and noise. However, not all the $\overline{\text{CMC}}^s_{\text{Dfree,r,i,k}}$ samples are used to compute the airborne multipath models. Instead, only samples every 2τ seconds are used in order to ensure sample independence as proposed in Harris et al. (2017). Then, these independent samples are organized into elevation bins of $5°$. For this purpose, satellite elevation in ECEF coordinates is used instead of the aircraft body frame. This approach is based on the assumption that the aircraft computes the expected multipath for a given satellite using the model and the elevation as determined by the receiver in ECEF coordinates, rather than converting it to the body frame elevation, as per aircraft manufacturers' guidelines.

For each bin, the root-mean-square (RMS) value is computed. It is important to note that while the RMS and standard deviation (STD) are equivalent when the mean in a bin is zero, RMS is chosen here to ensure conservativeness in cases where the mean of certain bins may not be zero due to the sample size. For simplicity, in this work, we use the same notation for both,

$\sigma_{CMC_{Dfree}}$. Note that, for the derivation of the airborne multipath models, only the samples after filter convergence are utilized. Consequently, observations from the initial 2τ seconds are excluded from binning and subsequent multipath model computation.

To achieve an accurate estimate of the multipath, it is important to remove the receiver's thermal noise. Harris et al. (2020) computed the standard deviation of thermal noise for the Collins GLU-2100 receiver, which is the same MMR prototype used in the DUFMAN study. Figure 4 shows the resulting thermal noise standard deviation for 100-second smoothed measurements as a function of elevation, along with the requirements for the receiver Airborne Accuracy Designator B (AAD-B) as a reference. Note that the thermal noise of the Collins GLU-2100 receiver is significantly below the AAD-B requirement.

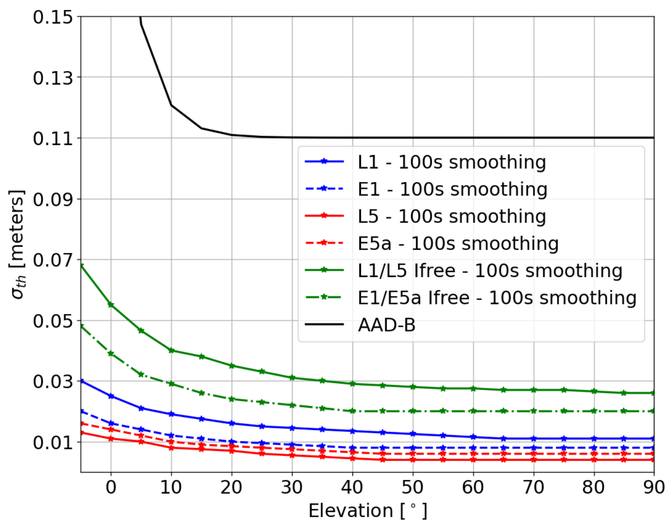

Figure 4: Receiver noise standard deviation versus elevation for 100-seconds smoothing.

Additionally, as the smoothing times considered might be shorter or longer than 100 seconds, the standard deviation of the receiver's thermal noise is modified accordingly, typically multiplying by a factor that takes into account the shorter or longer smoothing duration of the noise, $\sqrt{100/\tau}$ (Murphy et al. (2022, 2023)). Note that, for smoothing time constants exceeding 300 seconds, this factor might be overly optimistic, potentially resulting in less effective removal of thermal receiver noise. However, this approach would produce slightly higher multipath models, which are conservative and therefore would not compromise integrity.

Finally, the standard deviation of the receiver's thermal noise is subtracted from the root-mean-square (RMS) value per elevation bin (with θ representing the elevation bins in ECEF) as follows:

$$\sigma_{MP}(\tau,\theta) = \sqrt{\sigma^2_{CMC_{Dfree}}(\tau,\theta) - 100/\tau \cdot \sigma^2_{th}(100,\theta)} \tag{17}$$

8. Inflation considering the number of samples

The values derived from the measurements are based on a limited number of samples, and as such, the measured standard deviation or RMS does not directly represent the true standard deviation of the data. Additionally, when longer smoothing time constants are applied, the number of samples per bin decreases. To ensure the statistical representativeness of the data, an inflation factor computed per elevation bin is applied to the RMS in each bin derived from the limited data. This inflation factor, which adjusts the measurements-based RMS to account for their deviation from the true standard deviation, is determined using the chi-squared distribution as follows:

$$K_{infl}(\tau,\theta,\psi) = \sqrt{\frac{N_{indep}(\tau,\theta) - 1}{\chi^2_{N_{indep}}(\tau,\theta,\psi)}}, \tag{18}$$

with $N_{indep}(\tau,\theta)$ representing the effective number of independent samples used to derive the RMS in each elevation bin for each smoothing time constant τ, and $\chi^2_{N_{indep}}(\tau,\theta,\psi)$ representing the chi-square value with $N_{indep}(\tau,\theta) - 1$ degrees of freedom at a cumulative density function (CDF) equal to ψ, where ψ corresponds to one minus the desired confidence level (e.g., for a 95% confidence level, $\psi = 0.05$).

The reason for employing this formula is that the variance estimate from a finite number of samples follows a chi-squared distribution with $N_{indep} - 1$ degress of freedom. In this study, the 95% confidence bound is selected to provide reasonably conservative estimates without excessively inflating the model as proposed by Circiu et al. (2020a). However, it is important to note that the final result is not highly sensitive to the specific confidence bound, as the difference in the inflation factor across various confidence levels is minimal when a sufficient number of samples is collected.

The primary factor in determining the inflation factor is the number of independent samples in each elevation bin. As mentioned previously, the calculation of independent samples assumes that one observation every two time constants is independent, due to the transient behavior of the Hatch filter (Harris et al. (2017)).

The end result is an inflated value for the airborne multipath, free from antenna errors and receiver noise, which is used to assess the impact of the newly proposed DFMC GBAS architecture:

$$\sigma_{MP}(\tau, \theta) = K_{infl}(\tau, \theta, \psi) \cdot \sqrt{\sigma^2_{CMC_{Dfree}}(\tau, \theta) - 100/\tau \cdot \sigma^2_{th}(100, \theta)}. \tag{19}$$

IV. MULTIPATH INFLATION FACTOR FOR THE TRANSIENT PHASE OF THE FILTER

The transient phase of a smoothing filter begins with the filter's initialization and concludes when the filter reaches its steady state. For a time-variant filter, the steady state is typically achieved after a period of 2τ seconds of continuous operation.

To investigate the multipath behavior before reaching the steady state, the filters are re-initialized at intervals of 10 seconds, 20 seconds, and so on, up to a maximum duration (e.g., 1200 seconds or 2000 seconds). The data corresponding to each initialization is grouped and sorted into elevation bins, allowing to analyze the smoothing filter's behavior during its transient phase within each bin. Note that the data has not been reprocessed within the same parts. For instance, at a 30-second interval, the data from 0 to 30 seconds is processed, the filters are re-initialized, and the next part of raw multipath measurements is taken from $30 + \Delta t$ to 60 seconds. Therefore, the part from $0 + \Delta t$ to $30 + \Delta t$ is not processed again as in the case of using a sliding window. We selected this method because reprocessing the same data with a sliding window would provide samples that are somewhat correlated. Future work will explore an optimal moving window step size to obtain more samples while ensuring statistical independence.

Removing receiver thermal noise during this process presents challenges. Ideally, we would separately study the receiver noise behavior during the transient phase in order to later remove it from the smoothed multipath estimates during the transient phase. However, due to the limited availability of information (only the receiver information from Harris et al. (2020) was available), the receiver noise contribution was not removed. The reason behind is that the noise is relatively small and has significantly less impact compared to multipath effects during the transient phase of the filter.

The next step is to compute the ratio between the RMS of smoothed multipath after "t" seconds of elapsed time (e.g., after 10 seconds, 20 seconds, 30 seconds, etc., up to the maximum interval considered) and the RMS of smoothed multipath at the steady state for the smoothing time constant under study (e.g., 600 seconds). For this purpose, the samples that we used to calculate the transient state at each interval corresponded to the same satellite and epoch as those used for the steady state. If a sample at a given transient interval lacked a corresponding sample at steady state (e.g., 600 seconds), it was discarded.

With this ratio computed for each "t" seconds after filter re-initialization, we can derive an error inflation factor, $K_{transient}(t)$, to bound the ratio between the RMS of smoothed multipath errors during the transient phase at time "t" and the RMS of smoothed multipath errors at steady state (after the filter has converged).

The inflated multipath error at transient time t since filter re-initialization can be then obtained as:

$$\sigma_{MP,transient}(t) = K_{transient}(t) \cdot \sigma_{MP}(\tau, \theta(t)). \tag{20}$$

In this work, we derive the inflation factor based on the samples obtained as described above and a first-order error model that characterizes the behavior of time-variant smoothing filters, as proposed in Sgammini et al. (2022b); Blanch et al. (2019). This model accurately represents the transient and steady-state performance of the filters, allowing for a precise computation of the inflation factor during the transient phase as:

$$K_{transient}(t) = \sqrt{a_1 \cdot \left(\frac{1+\gamma}{(t+1)\cdot(1-\gamma)} - \frac{2\cdot\gamma}{(t+1)^2\cdot(1-\gamma)^2} \cdot (1-\gamma^{t+1}) \right) + a_2} \tag{21}$$

In Section V.2, we present the results of the derivation of this model with the real flight data.

V. RESULTS

1. Airborne multipath models for different smoothing time constants

Figure 5 presents the newly obtained results for the Dfree time-variant 100-second smoothed airborne multipath errors with respect to satellite elevation in ECEF coordinates (above the horizon) across different frequencies, compared to the current model for GPS L1 and the existing DUFMAN models. The blue-shaded region between the cyan and blue lines (where visible) represents the RMS values per bin with a 95% confidence bound.

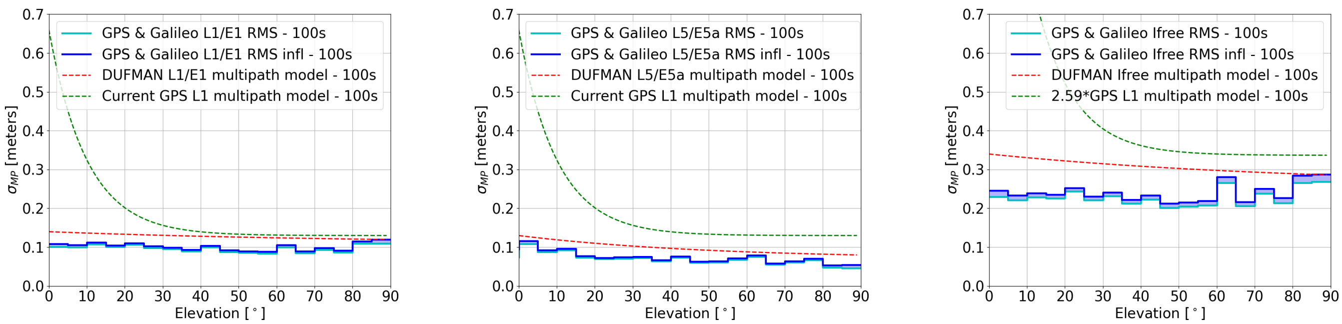

(a) L1/E1. **(b)** L5/E5a. **(c)** Ifree.

Figure 5: Dfree time-variant 100-seconds σ_{MP} computed per elevation bin for (a) L1/E1, (b) L5/E5a, and (c) Ifree. The red dashed line shows the current DUFMAN models, the dashed green line shows the current GPS L1 model, and the area between the blue curves represents the RMS values with a 95% confidence.

As can be observed, the newly derived RMS values are slightly lower than those of the current DUFMAN models for L1/E1 and Ifree. This reduction can be attributed to several factors. Firstly, the more accurate calibration of antenna errors, particularly for the L1/E1 frequency, allows for more efficient removal of AGDV errors from the multipath estimates, resulting in smaller overall RMS values. Secondly, more sensitive cycle slip detection reduces the likelihood of outliers or undetected cycle slips entering the smoothing filters, further contributing to the lower RMS values.

Additionally, for the derivation of these new models, we combined measurements from both GPS and Galileo for the same frequency, increasing the number of samples per elevation bin. This larger sample size per bin potentially reduces the overall standard deviation of the distribution, making it less susceptible to outliers. Notably, the blue area between the curves is almost imperceptible, indicating that the inflation factors used to account for the limited number of samples were close to one for nearly all bins. This suggests that a representative sample size was achieved in each bin.

The use of a time-variant filter also contributes to these results, as it requires less time for smoothed measurements to be utilized due to faster filter convergence, and fewer samples need to be skipped to maintain sample independence. However, peaks are observed in the high elevation bins for L1/E1, and especially for Ifree, which can be explained by a less representative number of samples in those bins, making the RMS values more susceptible to high multipath effects. Considering that the results are closely aligned, we propose to maintain the same model as proposed in DUFMAN for 100-second smoothing and L1/E1, L5/E5, and Ifree.

Figure 6 presents the results for the raw (unsmoothed) multipath errors across different frequencies, compared with the current model for GPS L1, the existing DUFMAN models, and the proposed RMS bounds for each frequency. The results indicate a more pronounced elevation dependency compared to the 100-second smoothing, primarily due to the influence of high-frequency multipath. Among the signals analyzed, the L5/E5a signal exhibits the lowest error, with a more significant difference from the L1/E1 signal than is observed after smoothing. This difference is expected, given the characteristics of L5/E5a signal compared to L1/E1.

Additionally, it is important to note that there is no observable difference between the inflated and uninflated curves regarding the number of samples. This is due to the robust sample size per bin in the raw data, ensuring the reliability of the statistical representation.

Figure 7 presents the results obtained using the Dfree time-variant smoothing filter with a smoothing time constant of 600 seconds across all frequencies. The results are compared with the proposed RMS-bound model, the current GPS L1 model, and the current DUFMAN models.

As can be observed, with the extended smoothing duration, the elevation dependency is almost negligible, as higher frequency multipath effects are effectively smoothed out. In this case, a noticeable difference between the inflated and uninflated curves is

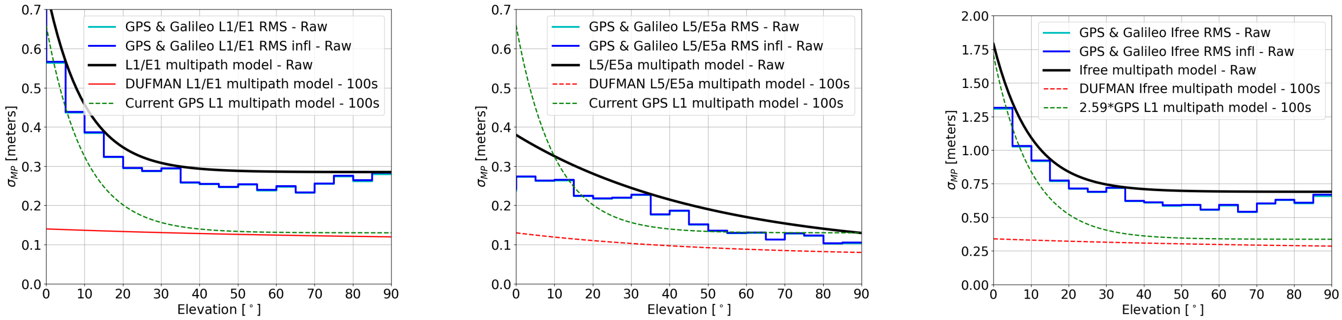

(a) L1/E1. **(b)** L5/E5a. **(c)** Ifree.

Figure 6: Unsmoothed σ_{MP} computed per elevation bin for (a) L1/E1, (b) L5/E5a, and (c) Ifree. The red dashed line shows the current DUFMAN models, the dashed green line shows the current GPS L1 model, the area between the blue curves represents the RMS values with a 95% confidence, and the continuous black line represents the proposed model for raw measurements.

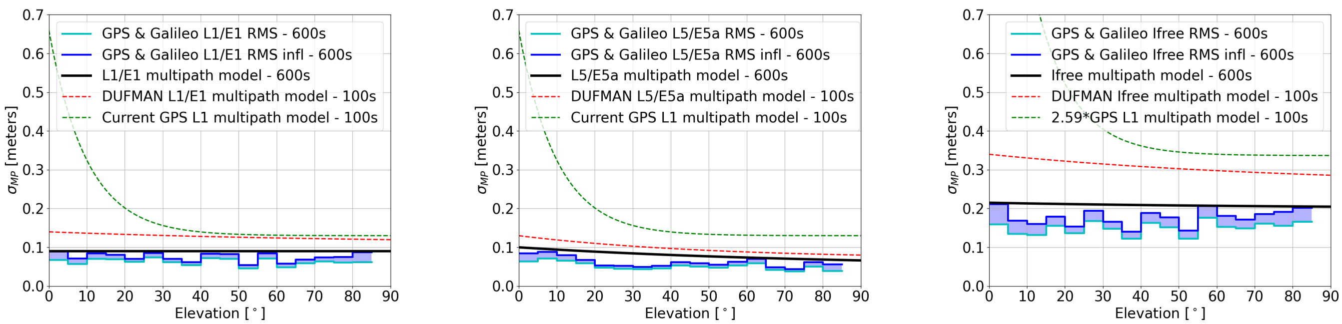

(a) L1/E1. **(b)** L5/E5a. **(c)** Ifree.

Figure 7: Dfree time-variant 600-seconds σ_{MP} computed per elevation bin for (a) L1/E1, (b) L5/E5a, and (c) Ifree. The red dashed line shows the current DUFMAN models, the dashed green line shows the current GPS L1 model, the area between the blue curves represents the RMS values with a 95% confidence, and the continuous black line represents the proposed model for 600 seconds smoothing.

observed, reflecting the significantly smaller sample size compared to the raw data case. Additionally, the difference between the L1/E1 and L5/E5a signals decreases with longer smoothing, and the Ifree model gets significantly lower than for 100 seconds smoothing.

Figures 8, 9, and 10 present all uninflated σ_{MP} curves for each frequency and smoothing time constant examined in this study. Figures 8a, 9a, and 10a show that the primary differences in smoothing are observed for time constants below 60 seconds. For smoothing time constants below 100 seconds, there is an elevation dependency, which is more visible for the L5/E5a frequency than for L1/E1 or Ifree. In the highest elevation bins, specifically those above 80 degrees, the RMS values increase once again for L1/E1 and Ifree, reaching values close to the ones at low elevation bins. This increase can be attributed to the reduced number of samples for high-elevation satellites, which affects statistical reliability.

Figures 8b, 9b, and 10b show that, for smoothing time constants exceeding 100 seconds, differences between curves are small, with nearly negligible variations observed particularly after 300 seconds of smoothing. The primary remaining differences are due to the sample size per bin, which impacts the statistical results, as seen with some anomalies, such as the 500-second smoothed σ_{MP} showing values lower than the 600-second smoothed σ_{MP} for the 80 to 90-degree elevation bin for L1/E1 and Ifree. For the L1/E1 and Ifree frequencies, the elevation dependency nearly disappears for these smoothing times. However, for L5/E5a, some elevation dependency is still visible, though the differences between smoothing times beyond 300 seconds are minor and similarly affected by the sample size in each bin.

Given the particular issues mentioned earlier, such as the influence of sample size in high elevation bins on statistical reliability, fitting models to all the σ_{MP} curves would be impractical, as this could result in overly conservative models. Therefore, Table 1 below presents values for the previously shown models: unsmoothed and 600 seconds. The 100 seconds model is the same as the one proposed in DUFMAN and therefore, it is not repeated in the table.

For the remaining smoothing time constants, a comprehensive strategy must be developed in collaboration with standardization

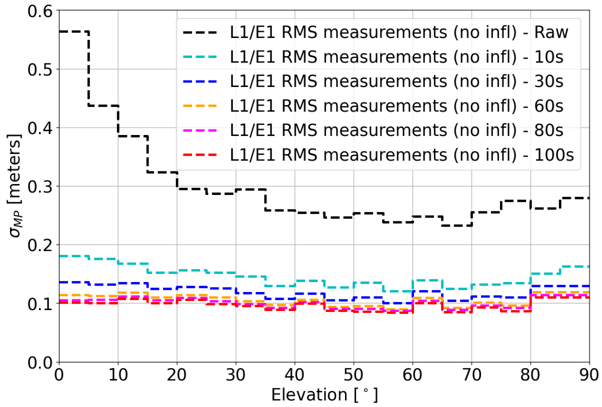

(a) Smoothing time constants below 100 seconds.

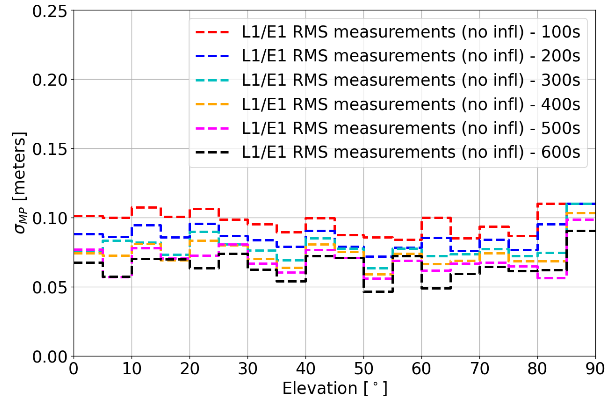

(b) Smoothing time constants above 100 seconds.

Figure 8: Dfree time-variant L1/E1 σ_{MP} computed per elevation bin for (a) smoothing time constants below 100 seconds, and (b) smoothing time constants above 100 seconds.

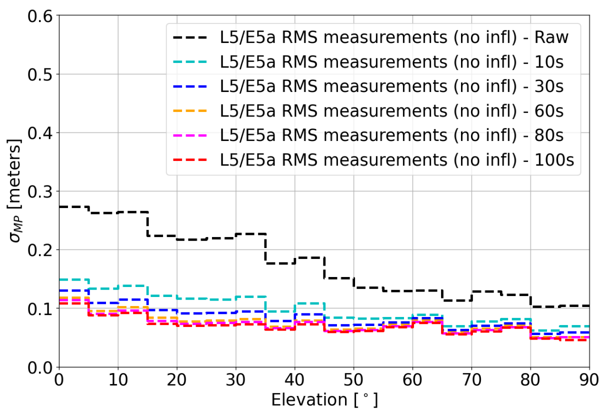

(a) Smoothing time constants below 100 seconds.

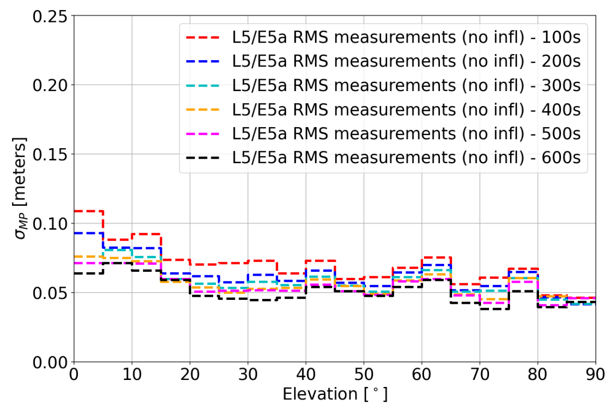

(b) Smoothing time constants above 100 seconds.

Figure 9: Dfree time-variant L5/E5a σ_{MP} computed per elevation bin for (a) smoothing time constants below 100 seconds, and (b) smoothing time constants above 100 seconds.

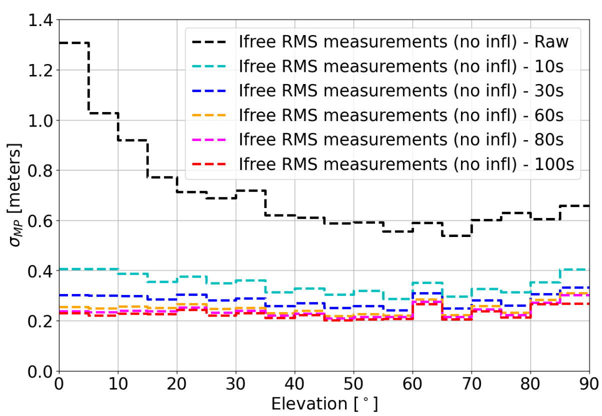

(a) Smoothing time constants below 100 seconds.

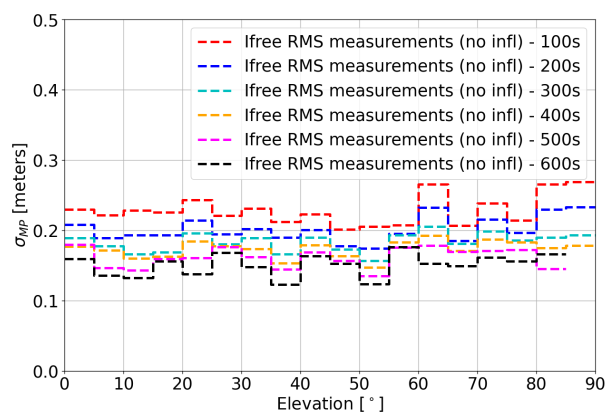

(b) Smoothing time constants above 100 seconds.

Figure 10: Dfree time-variant Ifree σ_{MP} computed per elevation bin for (a) smoothing time constants below 100 seconds, and (b) smoothing time constants above 100 seconds.

groups and airborne receiver manufacturers, as it is unlikely that airborne receivers will implement models for all possible smoothing time constants. A potential strategy is to define a reference airborne multipath model, such as the 100-second or 600-second model, and establish a method to derive models for other smoothing time constants based on the reference model, potentially through the use of an inflation factor. This is a challenging task since, as the smoothing time constant increases, the elevation dependency tends to flatten and differs across smoothing time constants. In future work, we will investigate the relationship between the converged models for different smoothing time constants and the inflation factor applied during the transient phase to determine whether a similar approach can be employed in this context.

Table 1: Airborne multipath models for unsmoothed and 600 seconds smoothed multipath.

Smoothing time constant	Model L1/E1	Model L5/E5a	Model Ifree
0 s (Unsmoothed)	$0.285 + 0.47 \cdot e^{(-El_{ECEF}/10)}$	$0.08 + 0.3 \cdot e^{(-El_{ECEF}/50)}$	$0.69 + 1.1 \cdot e^{(-El_{ECEF}/10)}$
600 s	0.091	$0.05 + 0.05 \cdot e^{(-El_{ECEF}/80)}$	$0.2 + 0.015 \cdot e^{(-El_{ECEF}/80)}$

2. Error behavior during the transient phase of the filter with respect to 600-seconds smoothing

To compute the multipath inflation factors during the transient phase of the filter, the data was sorted into elevation bins with a size of 10 degrees. Exceptions were made for elevations within the range of [0, 20] and [70, 90] degrees, which were grouped into single bins. This approach is justified by the typically scarce number of measurements at elevations below 10 degrees and higher than 80 degrees. By combining them with the nearest elevation bin, the statistical significance of these measurements is enhanced.

Figure 11a shows the error increase during the transient phase of the time-variant filter with respect to the 600-second L1/E1 smoothed multipath error at steady state for each elevation bin. The different curves represent the various elevation bins, where the satellite elevation is measured in the ECEF coordinate system (relative to the horizon). The orange curve indicates the inflation factor, which serves as an upper bound for all the curves. Note that the orange curve is not perfectly fitting the lowest elevation bin represented in dark blue. This is because the orange curve is also bounding the ratio at 0 seconds of smoothing or "unsmoothed multipath" for which the ratio is 6.33. The cyan curve represents the fitted model to the ratio derived from the bin with the highest error, corresponding to the lowest elevation bin.

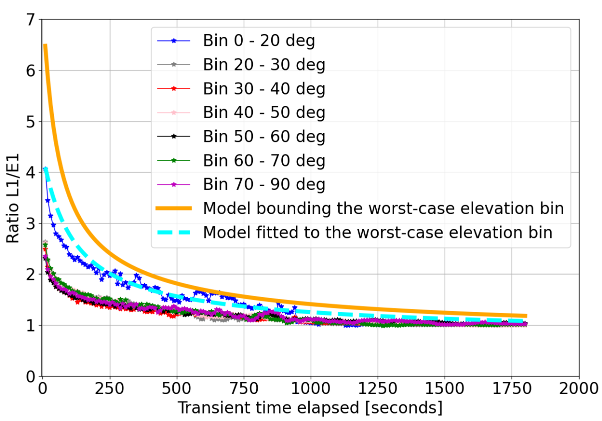

(a) Ratio for each elevation bin.

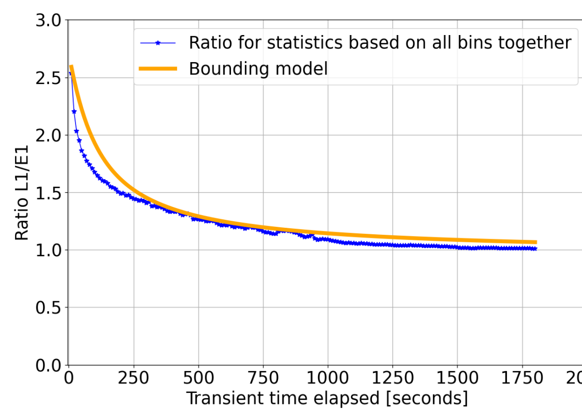

(b) Ratio for all elevation bins together.

Figure 11: Ratio of the increase of the RMS of the multipath error in the time-variant filter transient phase for L1/E1 with respect to the 600 seconds RMS.

Figure 11b shows the increase in error during the transient phase of the time-variant filter, compared to the 600-second L1/E1 smoothed multipath error at steady state, shown in blue, when combining samples from all elevations (i.e. computing the RMS for all samples per step of elapsed time without distinguishing per elevation bin). As observed, the combined behavior across all elevation bins closely matches that of individual bins with elevations above 20 degrees. This similarity can be attributed to the fact that in the time-variant filter, the initial samples have a higher weight than in the time-invariant filter, causing any significantly high unsmoothed multipath (especially prevalent at lower elevations) to have a more pronounced impact during the filter's transient phase. At higher elevations, where the effect of multipath is generally smaller, even in unsmoothed multipath, the behavior aligns more closely with the results obtained when computing statistics for all bins together. Table 2 presents the parameters to compute the inflation factor according to Equation (21) for all cases, including the conservative bound of the highest ratio (orange curve in Figure 11a), the fit of the highest ratio (cyan curve in Figure 11a), and the bound across all samples (orange curve in Figure 11b).

Figure 12a shows the error increase during the transient phase of the time-variant filter with respect to the 600-second L5/E5a smoothed multipath error for each elevation bin. Figure 12b shows the increase in error during the transient phase of the time-variant filter, compared to the 600-second L5/E5a smoothed multipath error, shown in blue, when combining all samples.

As observed, for L5/E5a, the lowest elevation bin was less affected by multipath, resulting in a slightly smaller bounding inflation factor, as indicated by the orange curve in Figure 12a. Similar to the previous analysis, the combined behavior across all samples closely aligns with that of individual bins with elevations above 20 degrees, due to the same underlying reasons discussed earlier. Table 2 presents the parameters to compute the inflation factor according to Equation (21) for all cases, including the conservative bound of the highest ratio (orange curve in Figure 12a), the fit of the highest ratio (cyan curve in Figure 12a), and the bound across all samples (orange curve in Figure 12b).

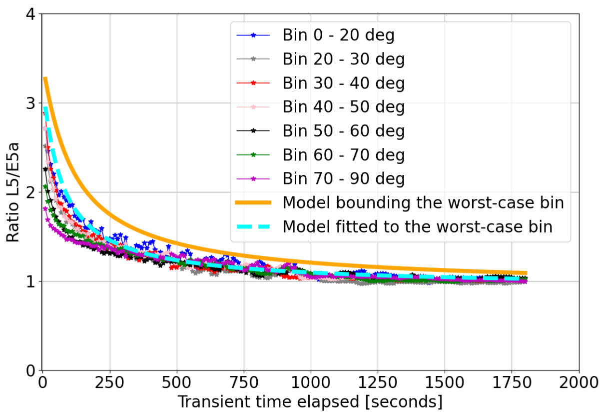

(a) Ratio for each elevation bin.

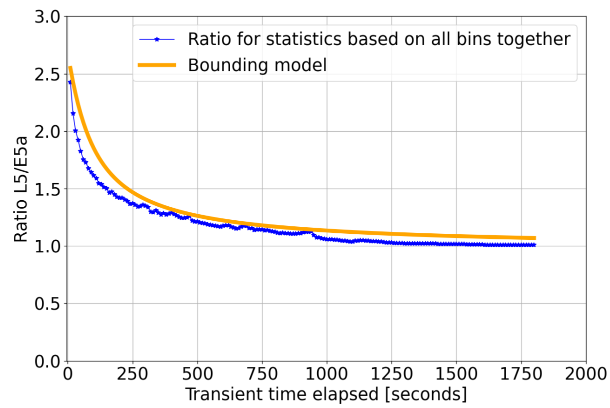

(b) Ratio for all elevation bins together.

Figure 12: Ratio of the increase of the RMS of the multipath error in the time-variant filter transient phase for L5/E5a with respect to the 600 seconds RMS.

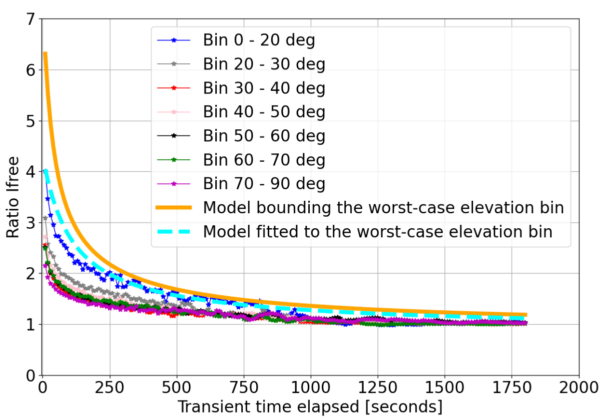

(a) Ratio for each elevation bin.

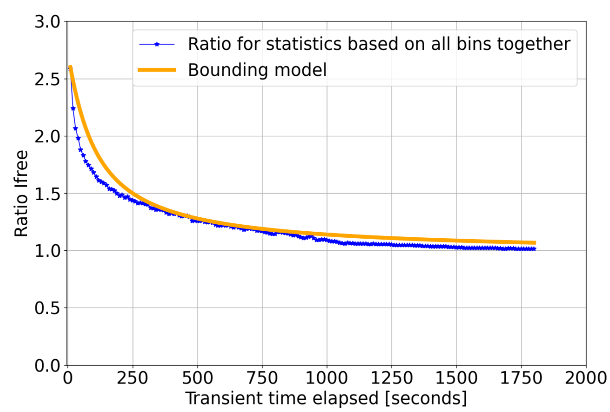

(b) Ratio for all elevation bins together.

Figure 13: Ratio of the increase of the RMS of the multipath error in the time-variant filter transient phase for Ifree with respect to the 600 seconds RMS.

Figure 13a shows the increase in error during the transient phase of the time-variant filter relative to the 600-second Ifree smoothed multipath error for each elevation bin. Figure 13b shows the increase in error during the transient phase of the time-variant filter, compared to the 600-second Ifree smoothed multipath error, shown in blue, when combining all samples.

The behavior of the Ifree smoothed multipath during the transient phase is quite similar to that of the L1/E1, as can be observed while comparing Figures 11a and 13a. This is because the dominant errors here come from L1/E1 and the lowest elevation bin. When using all samples, the ratios for all three cases (L1/E1, L5/E5a, and Ifree) exhibit similar patterns and values, suggesting that this behavior is more influenced by the characteristics of the filter than by the data itself.

Table 2 presents the parameters to compute the inflation factor according to Equation (21) for all cases, including the conservative bound of the highest ratio (orange curve in Figure 13a), the fit of the highest ratio (cyan curve in Figure 13a), and the bound across all samples (orange curve in Figure 13b).

Table 2: Parameters to compute the inflation factors during the transient phase of the filter.

Model	L1/E1	L5/E5a	Ifree
Bound of worst-case bin	$a_1 = 54.0$ $a_2 = 0.64$ $\gamma = 0.924$	$a_1 = 11.16$ $a_2 = 0.847$ $\gamma = 0.965$	$a_1 = 56.156$ $a_2 = 0.845$ $\gamma = 0.895$
Fit of worst-case bin	$a_1 = 18.5$ $a_2 = 0.64$ $\gamma = 0.962$	$a_1 = 9.56$ $a_2 = 0.862$ $\gamma = 0.945$	$a_1 = 18$ $a_2 = 0.764$ $\gamma = 0.96$
Bound of all samples	$a_1 = 6.5$ $a_2 = 0.92$ $\gamma = 0.968$	$a_1 = 6.329$ $a_2 = 0.961$ $\gamma = 0.963$	$a_1 = 6.6$ $a_2 = 0.937$ $\gamma = 0.965$

3. Error behavior during the transient phase of the filter with respect to 100-seconds smoothing

The previously presented results use the RMS of 600-second smoothed multipath at steady state as a reference. However, it remains unclear whether the appropriate reference model should be the 600-second converged model or the 100-second converged model, or which model the airborne receiver will actually implement. Since several applications (e.g., SBAS, ARAIM, and GBAS fallback modes) still rely on the 100-second smoothing airborne multipath model, it is anticipated that this model, at least, will be implemented in airborne receivers.

Therefore, our first approach was to repeat the analysis conducted in Section V.2 using the RMS of the 100-second smoothed multipath at steady state as a reference. The goal was to determine whether the 600-second smoothing model could be derived from the 100-second smoothing model directly, without the need to implement additional airborne multipath models in the airborne side.

However, in contrast to using as reference 600-seconds smoothed samples at steady state, when using 100-seconds smoothed samples as reference point, we cannot directly compare the filter output after "t" seconds of elapsed time with the steady state after 200 seconds (2τ). The reason behind is that, after this moment, the reference will contain a higher residual noise level (the time-variant filter for 100 seconds becomes time-invariant after convergence using $\alpha_k = \frac{\Delta t}{100}$) than the values we compare with (being smoothed with a changing $\alpha_k = \frac{\Delta t}{t}$ until 1200 seconds). This difference adds an unwanted random component to the result, which could lead to conservative inflation factors of 1 (using the same model for 100-seconds and 600-seconds). This approach is not ideal, as it would not adequately represent the benefits of using time constants longer than 100 seconds.

To overcome this issue, we performed an intermediate step to make both measures comparable. First, we computed the ratio between the RMS of the 100-second smoothed samples at steady state and the RMS of the 600-second smoothed samples at steady state, as shown by the red curves in Figures 14, 15, and 16. This ratio exhibits some variability due to the influence of sample size when reinitializing the filters (note that we only consider the same steady-state samples as in the transient phase study). To mitigate this, we computed the median overall transient elapsed time, indicated by the cyan dashed line in Figures 14, 15, and 16.

We then multiplied the inverse of the constant ratio between the 100-second and 600-second RMS at steady state by the ratio for the 600-second RMS during the transient phase for all samples combined (blue curves in Figures 11b, 12b, and 13b). The result is shown as black curves in Figures 14, 15, and 16. As expected, in all three cases (L1/E1, L5/E5a, and Ifree), the black curves cross 1 at approximately 200 seconds, which corresponds to the convergence time for the 100-second time-variant filter. If the final smoothing time constant were 100 seconds, the black curves would remain at 1 until the maximum transient time elapsed considered. However, since the smoothing time constant increases up to 600 seconds, the black curves decrease, ultimately

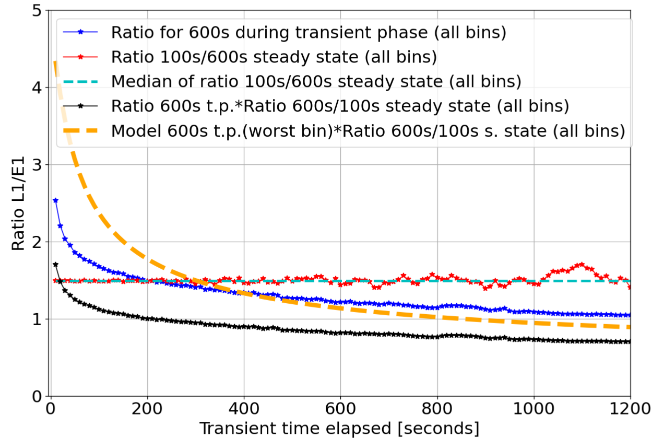

Figure 14: Ratio of the increase of the RMS of the multipath error in the time-variant filter transient phase for L1/E1 with respect to the 100 seconds RMS.

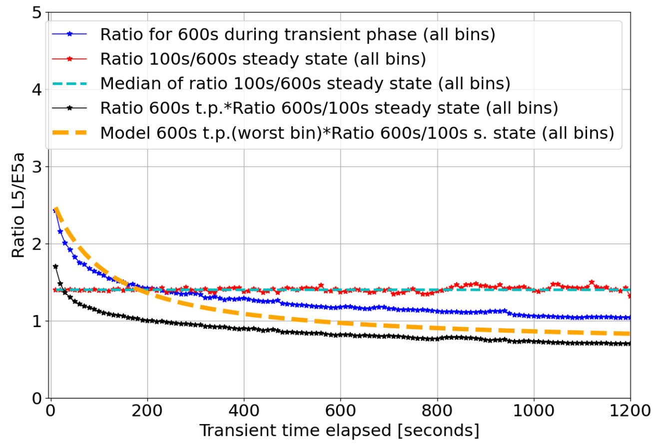

Figure 15: Ratio of the increase of the RMS of the multipath error in the time-variant filter transient phase for L5/E5a with respect to the 100 seconds RMS.

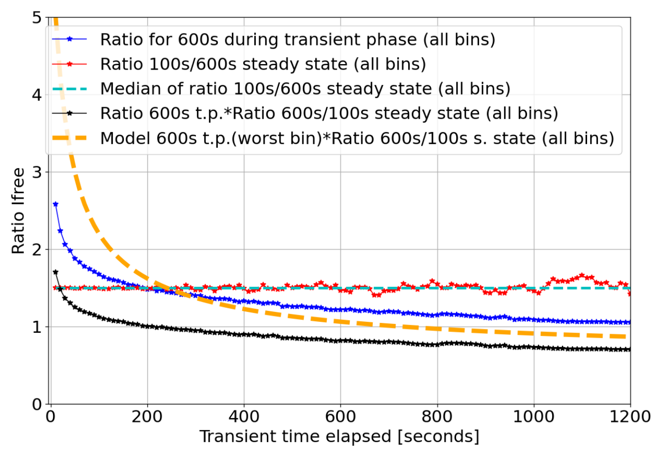

Figure 16: Ratio of the increase of the RMS of the multipath error in the time-variant filter transient phase for Ifree with respect to the 100 seconds RMS.

providing an approximate value of around 0.71 for L1/E1, L5/E5a and Ifree, which indicates how the 100-second model should be scaled to approximate the 600-second model at steady state.

Nevertheless, using this scaling factor directly with the DUFMAN 100-second models results in values that are smaller than the actual models for some elevation bins and smoothing time constants (e.g. unsmoothed multipath). This discrepancy arises because the scaling factor (black curve) is based on all the samples, and does not account for the worst-case scenarios of individual bins. Another more conservative approach could be multiplying the most conservative model (bounding the lowest elevation bin, represented by the orange curves in Figures 11a, 12a, and 13a) by the inverse of the ratio between the 100-second and 600-second RMS. This results in the orange dashed line in Figures 14, 15, and 16. As observed, this approach is notably conservative, applying a factor of around 0.875 to the DUFMAN models for L1/E1, L5/E5a, and Ifree to approximate the 600-second model.

Future work will focus on deriving a realistic factor to obtain other models from the 100-second model, balancing between the optimistic results represented by the black curves and the conservative results indicated by the orange curves.

VI. CONCLUSIONS

In this work, current airborne multipath models have been extended to support the standardization of DFMC GBAS. The revised methodology demonstrated that using a divergence-free filter alone would not change the existing models, as the previously utilized inputs were already divergence-free code-minus-carrier observables. The methodology also incorporated time-variant filters, which reduces convergence time to approximately 2τ. Enhancements to the original methodology proposed in the DUFMAN project included more sensitive cycle slip detectors, re-measurement of the flight campaign antenna for more accurate removal of antenna errors, and the combination of GPS and Galileo data to increase sample sizes. Additionally, inflation factors were applied to account for the reduced number of samples with longer smoothing time constants.

The derivation of models for different smoothing time constants yielded several key results. First, the two main factors driving the final model values are the calibration of antenna errors and the combination of Galileo and GPS data. These improvements resulted in a slightly smaller 100-second divergence-free time-variant model compared to previous models for 100-second smoothing. However, to account for the number of samples used, it is recommended to maintain the same 100-second models proposed in the DUFMAN project. Models for unsmoothed multipath and 600-second smoothed multipath were also developed. The model for 600-second smoothing was smaller than for 100-seconds smoothing as expected. Also, only small differences are visible after 300-seconds smoothing and all cases under study (L1/E1, L5/E5a, and Ifree). The values of the unsmoothed multipath model are highly dependent on measurement quality, receiver parameters, and other factors. One potential solution is to wait at least 10 seconds after filter initialization or satellite acquisition before using the measurements, and use the equivalent 10-seconds smoothing model instead.

For the behavior of smoothed multipath during the transient phase of the filter with respect to 600-seconds smoothing, different inflation factors were proposed. These include using a bound of the worst-case bin (lowest elevation bin), fitting the worst-case bin, or combining all samples together. We recommend the use of one of the first two methods together with the 600-seconds model after filter convergence, as combining all samples could result in overly optimistic resulting models.

We also studied the transient phase of the filter with respect to the 100-second smoothing models. To address this, we proposed a method to approximate the behavior of multipath during the transient phase of the filter with respect to 100-seconds smoothing by using the 600-second inflation factors and the steady-state ratio between 100 and 600 seconds smoothed multipath. Optimistic and conservative options were provided in this context as well.

Future work will further investigate the transient phase of filters relative to the selected reference model at the airborne side, with the goal of providing realistic models that are neither overly optimistic nor excessively conservative. Therefore, it is crucial for the aviation community to reach a consensus on which airborne multipath model (100 seconds, 600 seconds, both, or more) should be implemented in airborne systems.

ACKNOWLEDGEMENTS

The work presented in this paper was carried out in the frame of the project EDGAR (EGNSS DFMC GBAS bAsed opeRations) co-funded by EUSPA (European Union Agency for the Space Programme). Opinions expressed herein are those of the authors only and do not represent the contracting authorities' official position.

The authors would also like to thank the European Commission (EC) for providing the data collected during project DUFMAN (Dual Frequency Multipath Model for Aviation) and Dr. Simona Circiu for her invaluable advice and guidance during the course of this work.

REFERENCES

Blanch, J., Walter, T., and Phelts, R. E. (2019). Development and evaluation of airborne multipath error bounds for L1-L5. In *Proceedings of the 2019 International Technical Meeting of The Institute of Navigation*, pages 53–61.

Boeing (2005). Volume III: Multipath Flight Test Program Results. Technical report.

Booth, J., Murphy, T., Clark, B., and Liu, F. (2000). Validation of the airframe multipath error allocation for local area differential GPS. In *Proceedings of the IAIN World Congress and the 56th Annual Meeting of The Institute of Navigation (2000)*, pages 689–698.

Braasch, M. S. (1994). Isolation of GPS Multipath and Receiver Tracking Errors. *Navigation*, 41(4):415–435.

Caizzone, S., Circiu, M.-S., Elmarissi, W., Enneking, C., Felux, M., and Yinusa, K. (2017). Effect of antenna pattern uniformity on the pseudorange tracking error. In *Proceedings of the 30th International Technical Meeting of the Satellite Division of the Institute of Navigation (ION GNSS+ 2017)*, pages 3460–3470.

Caizzone, S., Circiu, M.-S., Elmarissi, W., Enneking, C., Felux, M., and Yinusa, K. (2019). Antenna influence on global navigation satellite system pseudorange performance for future aeronautics multifrequency standardization. *NAVIGATION*, 66(1):99–116.

Circiu, M.-S. (2020). *Integrity Aspects for Dual-frequency Dual-Constellation Ground Based Augmentation System (GBAS)*. Dissertation, RWTH Aachen.

Circiu, M.-S., Caizzone, S., Enneking, C., Fohlmeister, F., Rippl, M., Meurer, M., Felux, M., Gulie, I., Rüegg, D., Griggs, J., et al. (2021). Final Results on Airborne Multipath Models for Dualconstellation Dual-frequency Aviation Applications. In *Proceedings of the 2021 International Technical Meeting of The Institute of Navigation*, pages 714–727.

Circiu, M.-S., Caizzone, S., Felux, M., Enneking, C., Rippl, M., and Meurer, M. (2020a). Development of the dual-frequency dual-constellation airborne multipath models. *NAVIGATION*, 67(1):61–81.

Circiu, M.-S., Felux, M., Caizzone, S., Enneking, C., Fohlmeister, F., Rippl, M., Gulie, I., Rueegg, D., Griggs, J., Lazzerini, R., et al. (2019). Initial results for dual constellation dual-frequency multipath models. In *Proceedings of the 32nd International Technical Meeting of the Satellite Division of The Institute of Navigation (ION GNSS+ 2019)*, pages 1401–1417.

Circiu, M.-S., Felux, M., Caizzone, S., Enneking, C., Fohlmeister, F., Rippl, M., Gulie, I., Rüegg, D., Griggs, J., Lazzerini, R., et al. (2020b). Airborne multipath models for dual-constellation dual-frequency aviation applications. In *Proceedings of the 2020 International Technical Meeting of The Institute of Navigation*, pages 162–173.

Durba, P. (2018). High level concept and modes for DFMC GBAS. Technical report, ICAO NSP, Joint Working Groups, 3rd Meeting, Working Paper 27.

Eurocae (2019). Minimum Operational Performance Standard for Galileo / Global Positioning System / Satellite-Based Augmentation System Airborne Equipment. Technical report.

Harris, M., Miltner, M., Murphy, T., Raghuvanshi, A., and van Graas, F. (2017). Bounding GPS L1 antenna group delay variation for GNSS landing system integrity. In *Proceedings of the 2017 International Technical Meeting of the Institute of Navigation*, pages 591–605.

Harris, M., Schlais, P., Murphy, T., Joseph, A., and Kazmierczak, J. (2020). GPS and GALILEO airframe multipath error bounding method and test results. In *Proceedings of the 33rd International Technical Meeting of the Satellite Division of The Institute of Navigation (ION GNSS+ 2020)*, pages 114–139.

International Civil Aviation Organization (2017). International Standards and Recommended Practices (SARPs). Annex 10 to the Convention of International Civil Aviation. Volume I -Radio Navigation Aids. Technical report.

Misra, P. and Enge, P. (2006). *Global Positioning System: Signals, Measurements and Performance Second Edition*. Massachusetts: Ganga-Jamuna Press.

Murphy, T., Harris, M., Balvedi, G., McGraw, G., Wichgers, J., Lavik, L., Topland, M., Tuffaha, M., and Saito, S. (2022). Availability of Iono Gradient Detection with Alternative Architectures for DFMC GBAS. In *Proceedings of the 35th International Technical Meeting of the Satellite Division of The Institute of Navigation (ION GNSS+ 2022)*, pages 12–33.

Murphy, T., Harris, M., Balvedi, G., McGraw, G., Wichgers, J., Lavik, L., Topland, M., Tuffaha, M., and Saito, S. (2023). Managing Long Time Constant and Variable Rate Carrier Smoothing for DFMC GBAS. In *Proceedings of the 36th International Technical Meeting of the Satellite Division of The Institute of Navigation (ION GNSS+ 2023)*, pages 925–946.

Murphy, T., Harris, M., Booth, J., Geren, P., Pankaskie, T., Clark, B., Burns, J., and Urda, T. (2005a). Results from the program for the investigation of airborne multipath errors. In *Proceedings of the 2005 National Technical Meeting of The Institute of Navigation*, pages 153–169.

Murphy, T., Harris, M., Geren, P., Pankaskie, T., Clark, B., and Burns, J. (2005b). More results from the investigation of airborne multipath errors. In *Proceedings of the 18th International Technical Meeting of the Satellite Division of The Institute of Navigation (ION GNSS 2005)*, pages 2670–2687.

Murphy, T., Harris, M., McGraw, G., Wichgers, J., Lavik, L., Topland, M., Tuffaha, M., and Saito, S. (2021). Alternative Architecture for Dual Frequency Multi-Constellation GBAS. In *Proceedings of the 34th International Technical Meeting of the Satellite Division of The Institute of Navigation (ION GNSS+ 2021)*, pages 1334–1374.

Radio Technical Commission for Aeronautics (2006). DO-301, Minimum Operational Performance Standards for Global Navigation Satellite System (GNSS) Airborne Active Antenna Equipment for the L1 Frequency Band. Technical report.

Radio Technical Commission for Aeronautics (2018a). DO-253D, Minimum Operational Performance Standards for GPS Local Area Augmentation System Airborne Equipment. Technical report.

Radio Technical Commission for Aeronautics (2018b). DO-373, Minimum Operational Performance Standards for GNSS Airborne Active Antenna Equipment for the L1/E1 and L5/E5a Frequency Bands. Technical report.

Radio Technical Commission for Aeronautics (2020). DO-229D, Minimum Operational Performance Standards for Global Positioning System/Satellite Based Augmentation System Airborne Equipment. Technical report.

Sanz, J., Juan, J., and Hernández-Pajares, M. (2013). *GNSS data processing, Vol. I: fundamentals and algorithms. ESA communications*. ESTEC TM-23/1, Noordwijk, Netherlands.

Sgammini, M., Caizzone, S., Blanco Delgado, N., Mabilleau, M., and Chatre, E. (2022a). Airborne Multipath and Antenna Error Models before Smoothing Filter Convergence. Technical report, ICAO NSP, Joint Working Groups, 9th Meeting, Information Paper 3.

Sgammini, M., Caizzone, S., Circiu, S., Rippl, M., Mabilleau, M., Delgado, N., and Chatre, E. (2022b). Airborne Multipath and antenna error models. Technical report, EUROCAE WG62.

Wanninger, L., Sumaya, H., and Beer, S. (2017). Group delay variations of GPS transmitting and receiving antennas. *Journal of Geodesy*, 91:1099–1116.

Wozniak, J. G. and Murphy, T. (1997). Multipath Modeling for Airborne and Ground Based Receivers Utilizing Flight Test Data. In *Proceedings of the 1997 National Technical Meeting of The Institute of Navigation*, pages 253–259.